Supporting information

for

Two-dimensional N-doped Pd/carbon for highly efficient heterogeneous catalysis

Jiuxuan Zhang,[a] Ze-Xian Low,[b] Yanhua Shao,[a] Hong Jiang*[a] and Rizhi Chen*[a]

[a] State Key Laboratory of Materials-Oriented Chemical Engineering, Nanjing Tech University, Nanjing 211816, Jiangsu, People's Republic of China

[b] Department of Chemical Engineering, Monash University, Clayton, Victoria 3800, Australia

*Corresponding author. hjiang@njtech.edu.cn; rizhichen@njtech.edu.cn

Experimental section

Materials

Cobalt nitrate hexahydrate ($Co(NO_3)_2•6H_2O$) and zinc nitrate hexahydrate ($Zn(NO_3)_2•6H_2O$) were purchased from Aladdin. 2-Methylimidazole (Hmim) was achieved from Sigma-Aldrich. Phenol (C_6H_5OH) was purchased from Sinopharm Chemical Reagent Co., Ltd.. Palladium chloride ($PdCl_2$, 99%) was obtained from Sin-platinum Metals Co., Ltd.. Methanol (MeOH) was purchased from Yonghua Chemical Technology (Jiangsu) Co., Ltd.. Cyclohexane was obtained from Shanghai Shenbo Chemical Co., Ltd.. The above chemicals were used as received without further purification. Deionized water (DI water) was self-produced.

Preparation of ZIFs

The preparation of ZIF-L was referred to the reported literature with a few alterations.[1] Briefly, we dissolved 0.1 mol of Hmim in 250 mL of DI water and kept stirring at room temperature. The metal aqueous solution (250 mL) was put into the above solution 10 min later. The mixture (molar ratio of M^{2+}: Hmim was 1:8) was stirred at 30 ^oC for 10 h. Finally, the lilac solid was centrifuged and washed with DI water, then dried at 70 ^oC for 6 h. The resultant ZIF-L with different molar ratios of Zn^{2+} and Co^{2+} are labeled as ZIF-L(x:y), corresponding to the molar ratios of Zn^{2+} and Co^{2+} (x:y = 1:0, 3:1, 1:1, 1:3, 0:1, respectively). The 3D ZIFs were synthesized by using methanol to replace DI water during the synthesis process, followed with the same purification process.

Preparation of ZIF-derived CN

The as-synthesized ZIF (0.5 g) was placed in a porcelain boat (60 mm × 120 mm), annealed in a tubular furnace under a flowing Ar (50 mL min^{-1}) at 750 ^oC for 2 h, and the corresponding

material is labeled as M/CN(x:y) (tips: the air in the tubular furnace should be remained without Ar replacement). ZIF-L(1:3) was pyrolyzed at different temperatures, and the corresponding samples are named as M/CN(1:3)-T (T=550, 600, 650, 750, 850 and 950, T refers to the pyrolysis temperature (^{o}C)). The product was etched thoroughly using nitric acid (30%) to remove the metals. After acid etching, the sample was washed with DI water several times until it was neutral, and then collected by filtration followed by drying at 70 ^{o}C overnight. The final sample is signed as CN(x:y)-T. When using the 3D ZIF-67(x:y) as the precursor, after calcination and pickling, the resultant material is marked as 3DCN(x:y)-650. All the materials without the post fixed T indicated that the calcination temperature was 750 ^{o}C.

Preparation of Pd@CN catalysts

A simple impregnation method was used to load Pd. In general, 0.2 g of support was added into $PdCl_2$ aqueous solution (15 mL, 0.45 g L^{-1}) with continuous stirring at 25 ^{o}C for 12 h. The $PdCl_2$ aqueous solution was prepared by dissolving $PdCl_2$ in hydrochloric acid with ultrasound (the molar ratio of $PdCl_2$: HCl was 1: 2) and then diluting with DI water. After that, the CN(x:y)-T supported Pd precursor was obtained by filtration and washing with DI water followed by drying at 70 ^{o}C overnight. Finally, the resulting product was annealed in a tubular furnace under a flowing of hydrogen at 250 ^{o}C for 5 h. The corresponding as-prepared Pd catalyst is labeled as Pd@CN(x:y)-T. Pd@3DCN(1:3)-650 was prepared by using 3DCN(1:3)-650 as the support via the same method.

Characterization

Powder X-ray diffraction (XRD) patterns of the as-prepared materials were obtained using a Rigaku MiniFlex 600 diffractometer. The morphologies of the samples were characterized via

scanning electron microscopy (SEM, Hitachi S-4800) and transmission electron microscopy (TEM, FEI Tecnai G2 F30). The elemental mapping was performed on Talos F200X to determine the distribution of C, O, N, Co, Zn and Pd. The Pd content of the catalyst was detected by an Optima 2000 DV ICP-OES. Textural characterization was performed on a Micromeritics ASAP 2020 system by nitrogen sorption isotherms, and the pore size distribution curves were obtained by the original Density Functional Theory method (DFT). Thermogravimetry-mass spectrum (TGA-MS) was obtained on a NETZSCH STA449-QMS403D F3 thermal analyzer under argon atmosphere. The surface composition and chemical structures of the catalysts were investigated by X-ray Photoelectron Spectroscopy (XPS, Thermo ESCALAB 250Xi), while the surface alkaline sites of the catalysts were identified by the CO_2 temperature-programmed desorption (CO_2-TPD) technique. The hydrophilicity was investigated by water contact angle (WCA) (Dropmeter A-100).

Evaluation of catalytic performance and phenol adsorption capacity

The catalytic performance of the as-prepared catalysts was tested in a 50 mL autoclave (Sen Long Instruments Company, Beijing, China) under atmospheric pressure (1 bar) of hydrogen. The reaction temperature was stabilized at 80 ^{o}C. Generally, a certain amount of catalyst (0.03 g) was added to phenol solution (20 mL, 1 wt. %), and the catalyst was filtrated after the reaction (Reaction time: 120 min). The concentrations of products and substrate were determined by GC-FID (Shimadzu, GC-2014), and the products were identified by GC-MS (Bruker, SCION-MS-4306GC) and NMR (NMR spectra were obtained on a JNM-ECZ400S spectrometer with $CDCl_3$ as solvents, 400 MHz).

The phenol adsorption capacities of the as-synthesized catalysts were evaluated under the same conditions of the evaluation of the catalytic performance, except that the hydrogen was

replaced by nitrogen.

The phenol conversion, cyclohexanone selectivity and phenol adsorption capacity were calculated by the following equations:

$$\text{Conversion}\ (\%) = \frac{(\text{Initial moles of phenol}) - (\text{Final moles of phenol})}{\text{Initial moles of phenol}} \times 100$$

$$\text{Selectivity}\ (\%) = \frac{\text{Moles of cyclohexanone}}{(\text{Initial moles of phenol}) - (\text{Final moles of phenol})} \times 100$$

$$\text{Adsorption capacity}\ (\%) = \frac{(\text{Initial moles of phenol}) - (\text{Final moles of phenol})}{\text{Initial moles of phenol}} \times 100$$

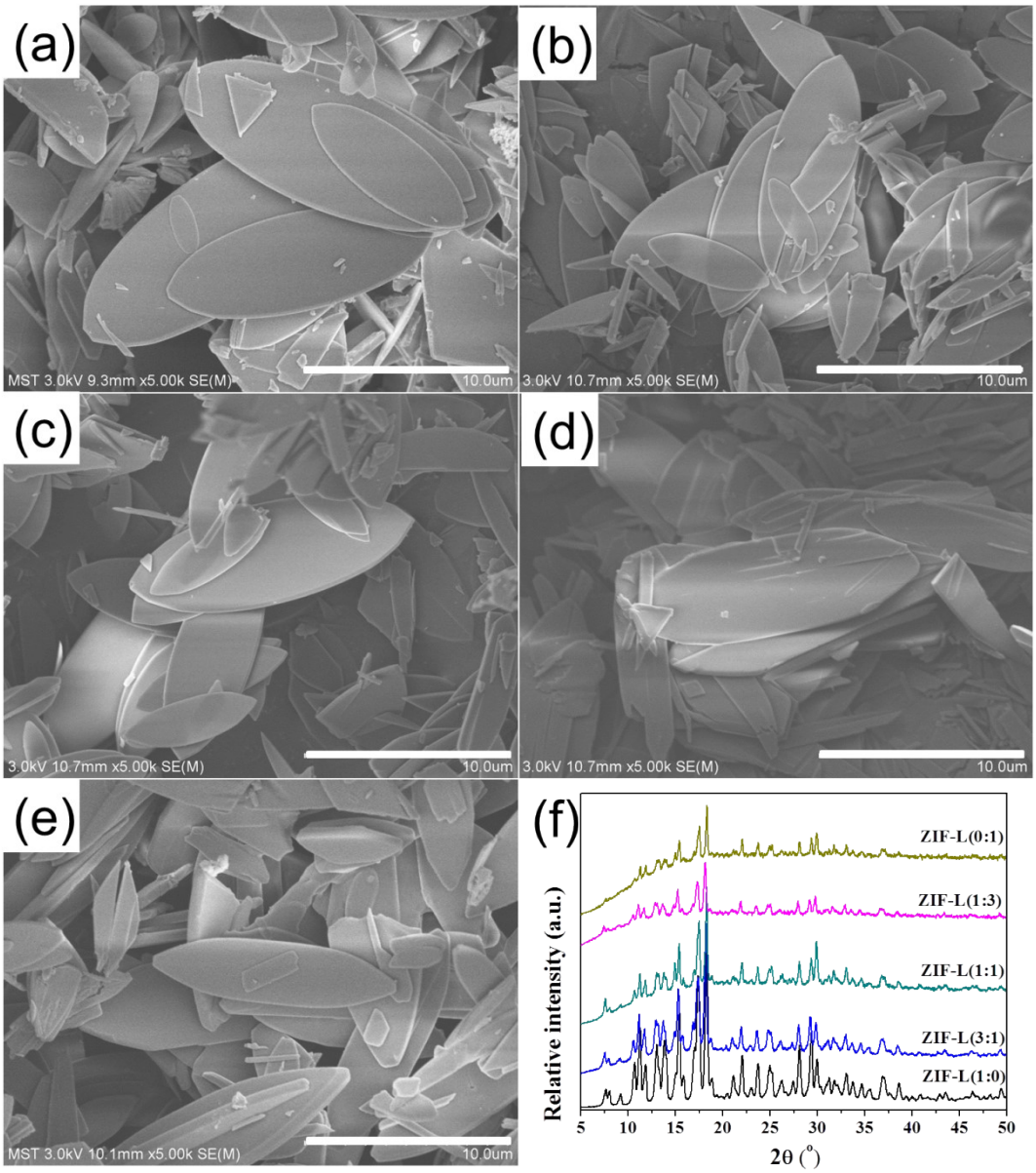

Figure S1. FESEM images of ZIF-L(x:y): (a) 1:0, (b) 3:1, (c) 1:1, (d) 1:3, (e) 0:1 (Scale bar= 10 μm). The corresponding XRD patterns (f)

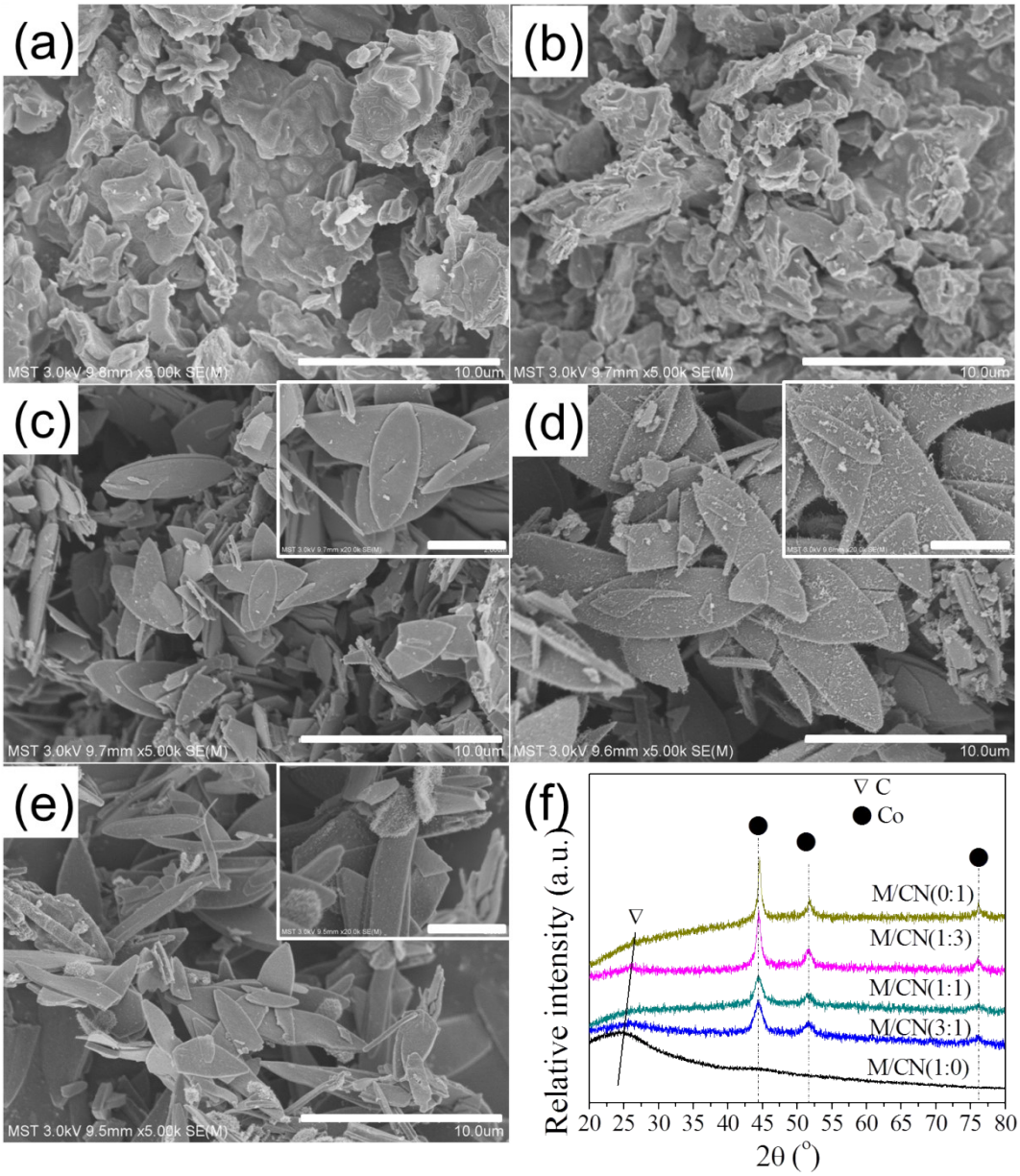

Figure S2. FESEM images of M/CN(x:y): (a) 1:0, (b) 3:1, (c) 1:1, (d) 1:3, (e) 0:1 (Scale bar= 10 µm) (Scale bar in embed images= 2 µm). The corresponding XRD patterns (f)

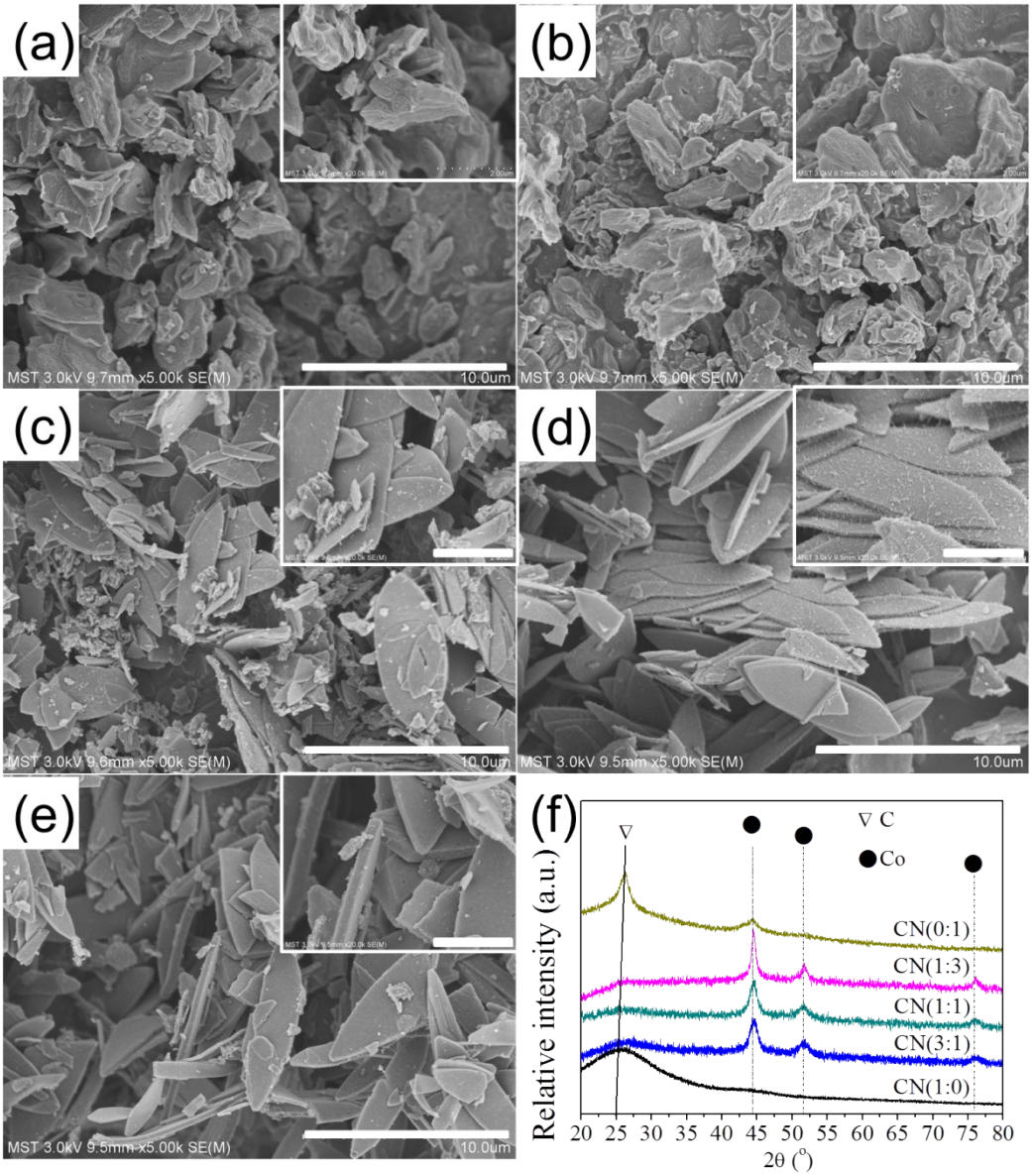

Figure S3. FESEM images of CN(x:y): (a) 1:0, (b) 3:1, (c) 1:1, (d) 1:3, (e) 0:1 (Scale bar= 10μm) (Scale bar in embed images = 2 μm). The corresponding XRD patterns (f)

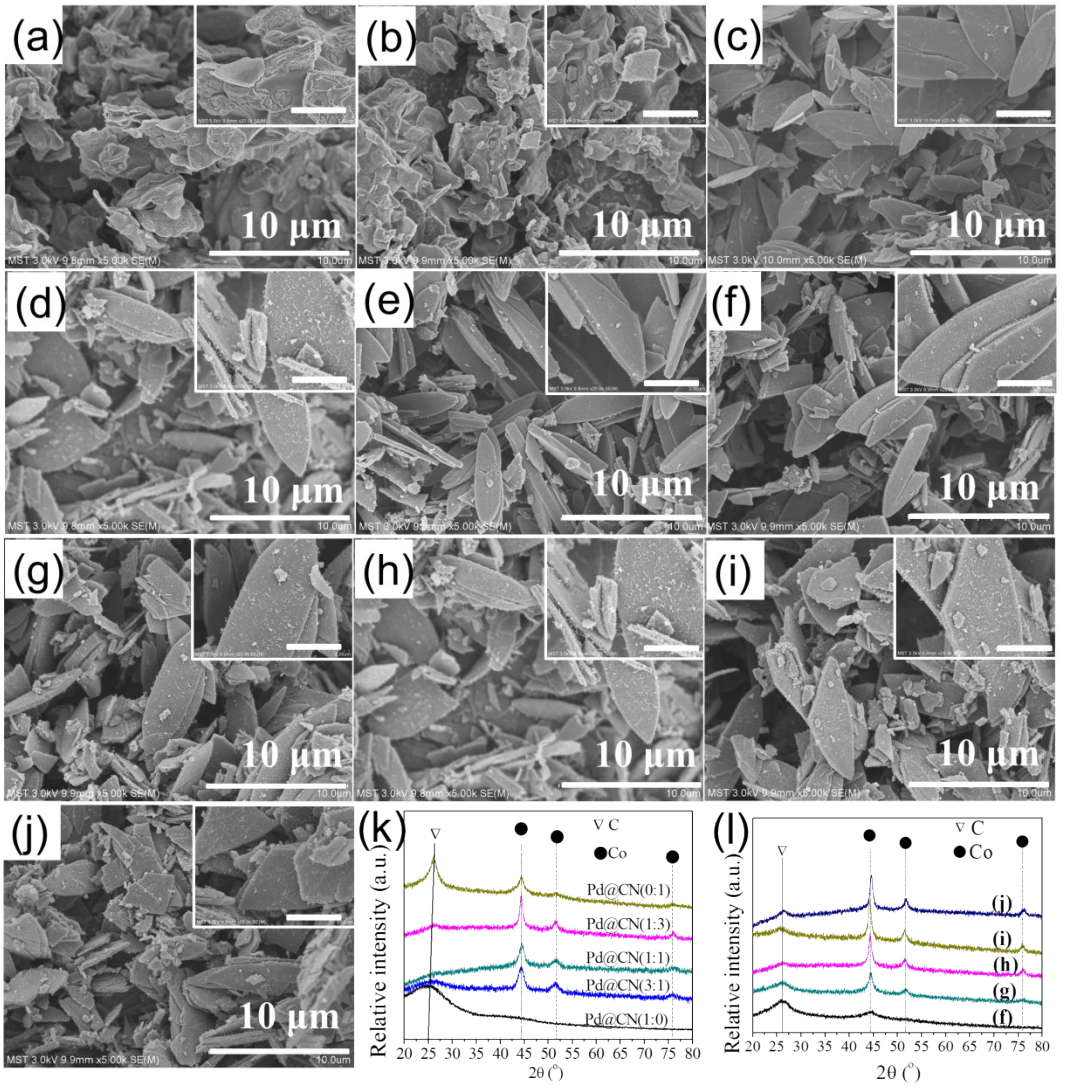

Figure S4. FESEM images of Pd@CN(x:y): (a) 1:0, (b) 3:1, (c) 1:1, (d) 1:3, (e) 0:1; FESEM images of Pd@CN(1:3)-T, T= (f) 550, (g) 650, (h) 750, (i) 850, (j) 950 °C (Scale bar in embed images= 2 μm). The corresponding XRD patterns of Pd@CN(x:y) (k) and Pd@CN(1:3)-T (l)

The Pd@CN(1:3)-T catalysts all maintain the leaf morphology with CNTs on the surface (**Figure** S4f-j). With the increase of calcination temperature, the leaf-like structure is gradually broken, but the 2D morphology keeps. The number and length of CNTs on the surface of Pd@CN(1:3)-T increase with the increase of calcination temperature, and Pd@CN(1:3)-850 exhibits the most amount of CNTs on the surface. When the calcination temperature is 950 °C, only some short CNTs are observed on the surface, probably Co NPs aggregate at higher temperature and decrease the catalytic performance of forming CNTs.

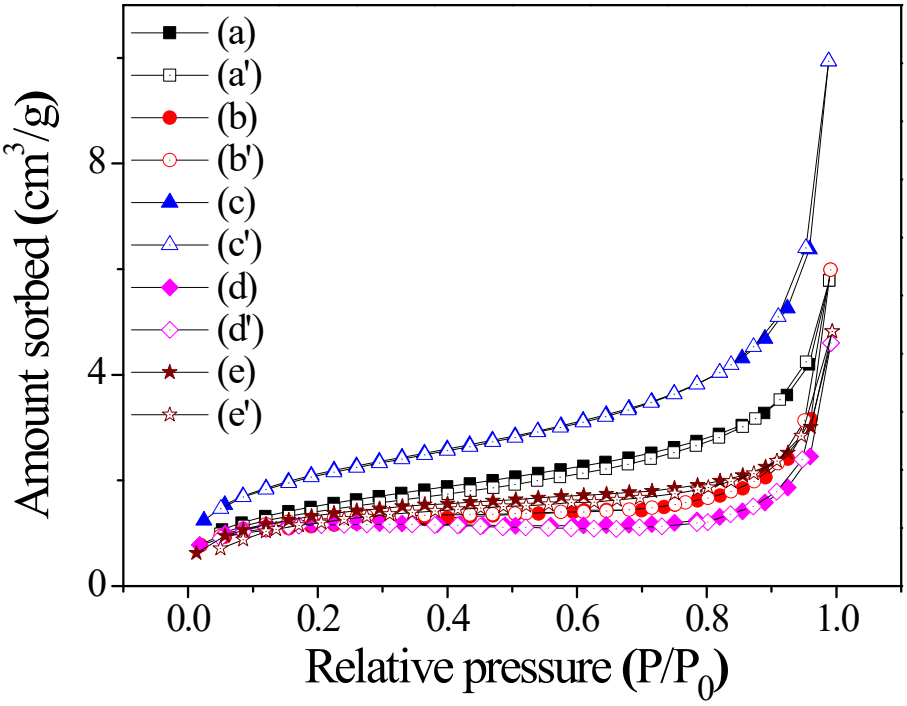

Figure S5. N_2 sorption isotherms of ZIF-L(x:y): (a) 1:0, (b) 3:1, (c) 1:1, (d) 1:3, (e) 0:1.

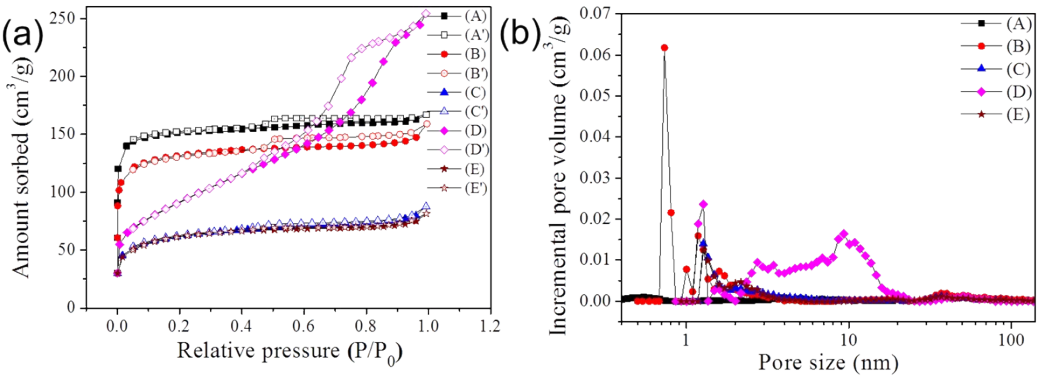

Figure S6. (a) N_2 sorption isotherms and (b) pore size distribution curves of M/CN(x:y): (A) (1:0), (B) (3:1), (C) (1:1), (D) (1:3), (E) (0:1)

The reasons for the formation of mesopores are as follows: 1. When the molar ratio of Zn is more than 50%, ZIF-L collapses and binds during the pyrolysis; 2. For other M/CN(x:y) materials, mesopores may be formed by the aggregation of Co NPs that leaves nanoscale pores in the original position,[2] and CNTs catalyzed by Co are also an important source of mesopores. As listed in **Table** S1, the specific surface areas of all Co-containing M/CN(x:y) (y >0) are lower than M/CN(1:0), which may be due to the fact that Co NPs grow up during the calcination and destroy the micropores in the ZIF-L frameworks. The pore volume of the Co-containing M/CN(x:y)

materials first increases and then decreases with the increase of Co ratio. Mesopores in M/CN(3:1) and M/CN(1:1) are less than M/CN(1:3) because the CNTs catalyzed by less and smaller Co NPs are shorter (**Figure** S2). The lower pore volume and mesoporous volume of M/CN(0:1) than M/CN(1:3) means that when there is no barrier of Zn, Co NPs are easy to agglomerate and grow into large particles, thereby reducing the capacity to catalyze the formation of CNTs (**Figure** S2 and **Table** S1).[3, 4] When the molar ratio of Zn is higher than 50%, the pores with diameter larger than 2 nm are very fewer. As the cobalt ratio increases, the number of large-size pores in M/CN(x:y) also increases, while the mesopores in M/CN(0:1) are lower than M/CN(1:3) owing to the less CNTs (**Figure** S2d, e).

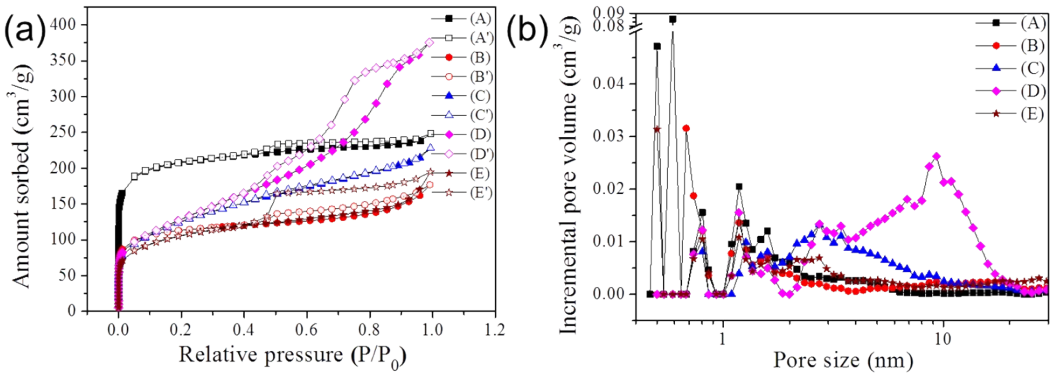

Figure S7. (a) N_2 sorption isotherms and (b) pore size distribution curves of Pd@CN(x:y): (A) (1:0), (B) (3:1), (C) (1:1), (D) (1:3), (E) (0:1)

The N_2 sorption isotherms of these catalysts all show similar type of isotherms with M/CN (**Figures** S6a and S7a). Compared to M/CN, the specific surface areas and pore volumes of all catalysts become larger, and the cavities left by the removal of metal are the source of new pores (**Tables** S1 and S2).[5] Pd@CN(1:3) has the largest total pore volume; in addition, the meso/macroporous volume also follows this variation trend, which is consistent with M/CN (**Tables** S1 and S2).

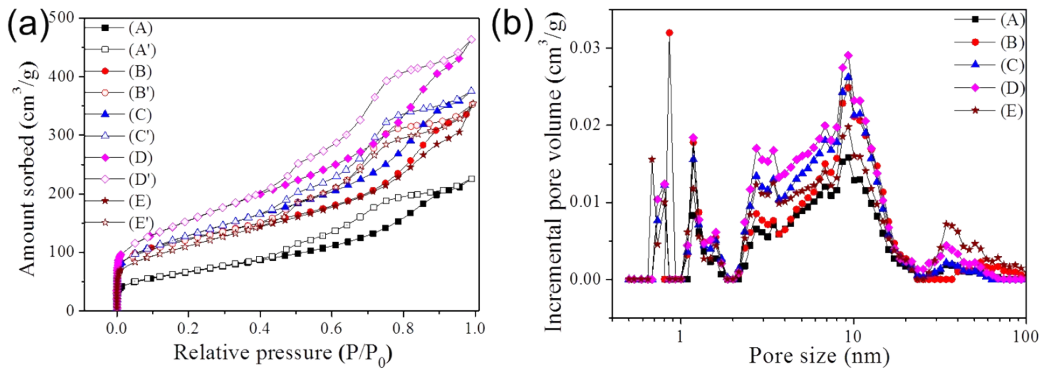

Figure S8. (a) N_2 sorption isotherms and (b) pore size distribution curves of Pd@CN(1:3)-T, T= (A) 550, (B) 650, (C) 750, (D) 850, (E) 950 °C.

When the calcination temperature is lower than 950 °C, more CNTs are produced on the surface of the Pd@CN(1:3)-T materials (**Figure** S4f-i), signifying more pores, which leads to the increase in the N_2 adsorption amount and specific surface area (**Figure** S8a and **Table** S3). When the calcination temperature reaches 950 °C, the Zn in the material volatilizes, and the layered structure and CNTs are destroyed, thus decreased specific surface area.[6] Calcination temperature has no effect on the pore size distribution range (**Figure** S8b).

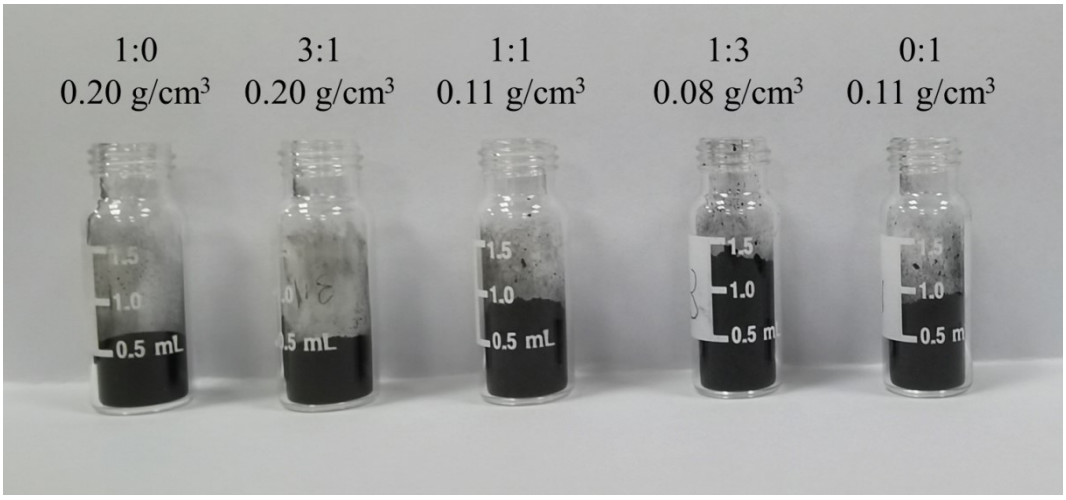

Figure S9. Comparison of the volumes occupied by 0.1 g of Pd@CN(x:y) in powder. (The density is the weight of catalysts to the volume)

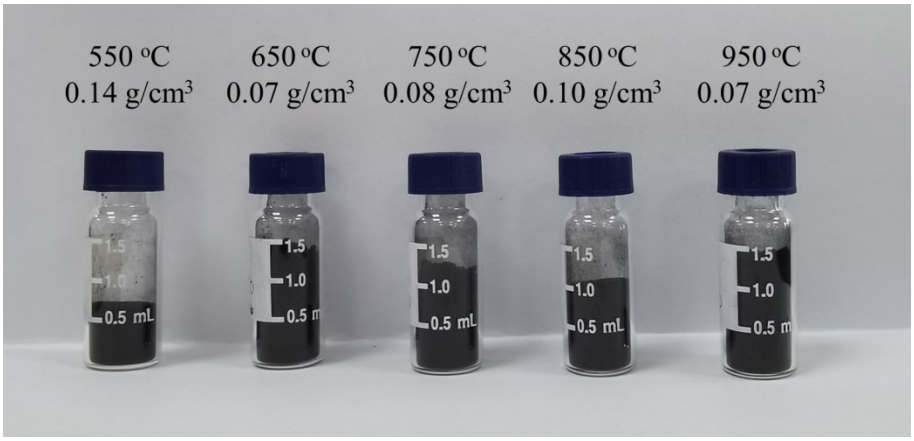

Figure S10. Comparison of the volumes occupied by 0.1 g of Pd@CN(1:3)-T catalysts in powder. (The density is the weight of catalysts to the volume)

The Co ratio and calcination temperature have a significant effect on the density of Pd@CN (**Figures** S9 and S10), and Pd@CN(1:3)-650 has the lowest density (0.07 g cm^{-3}). The difference in the density may be caused by the morphology, mesopores and the amounts of CNTs on the surface (**Figures** S4, S7 and S8).

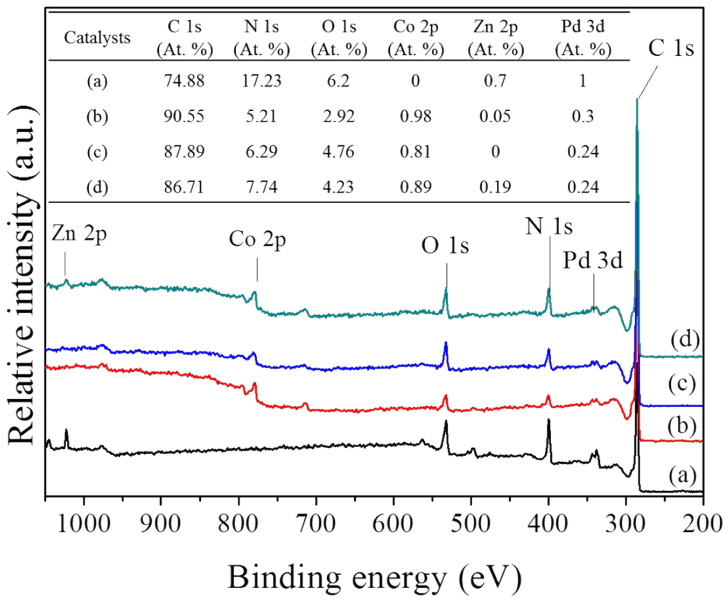

Figure S11. XPS results and survey spectra of Pd@CN(1:0) (a), Pd@CN(1:3) (b), Pd@CN(0:1) (c), Pd@CN(1:3)-650 (d)

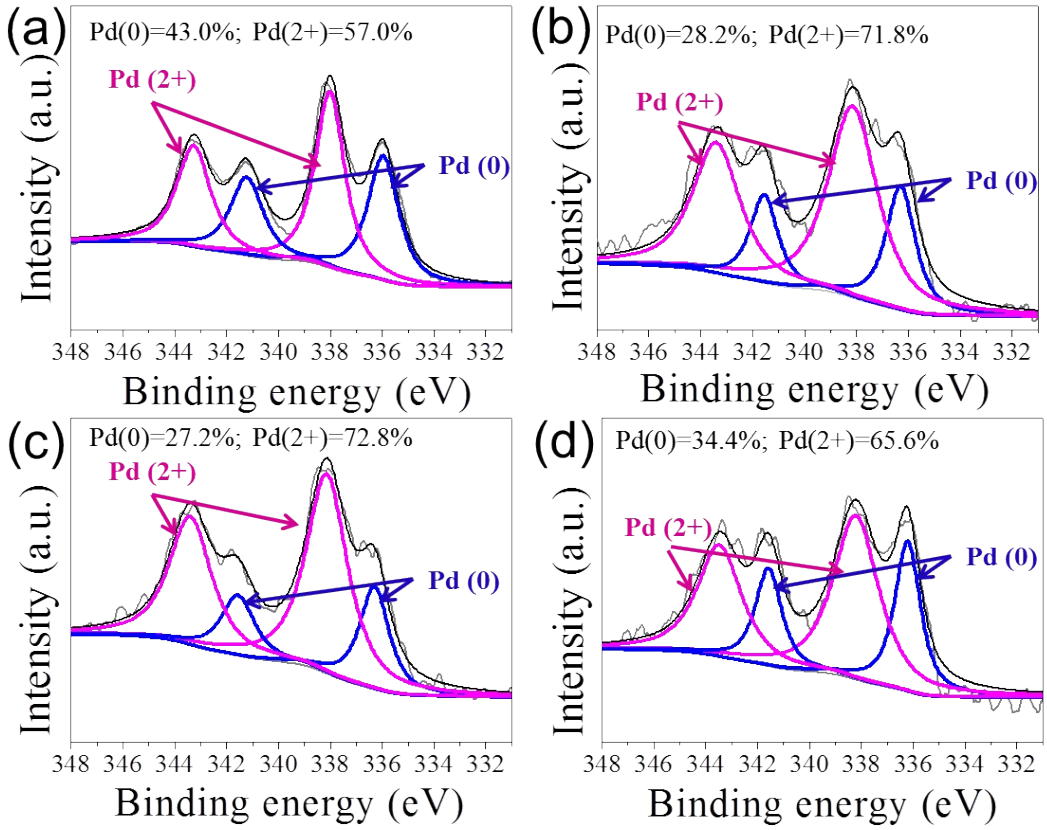

Figure S12. Pd 3d spectra of Pd@CN(1:0) (a), Pd@CN(1:3) (b), Pd@CN(0:1) (c), Pd@CN(1:3)-650 (d)

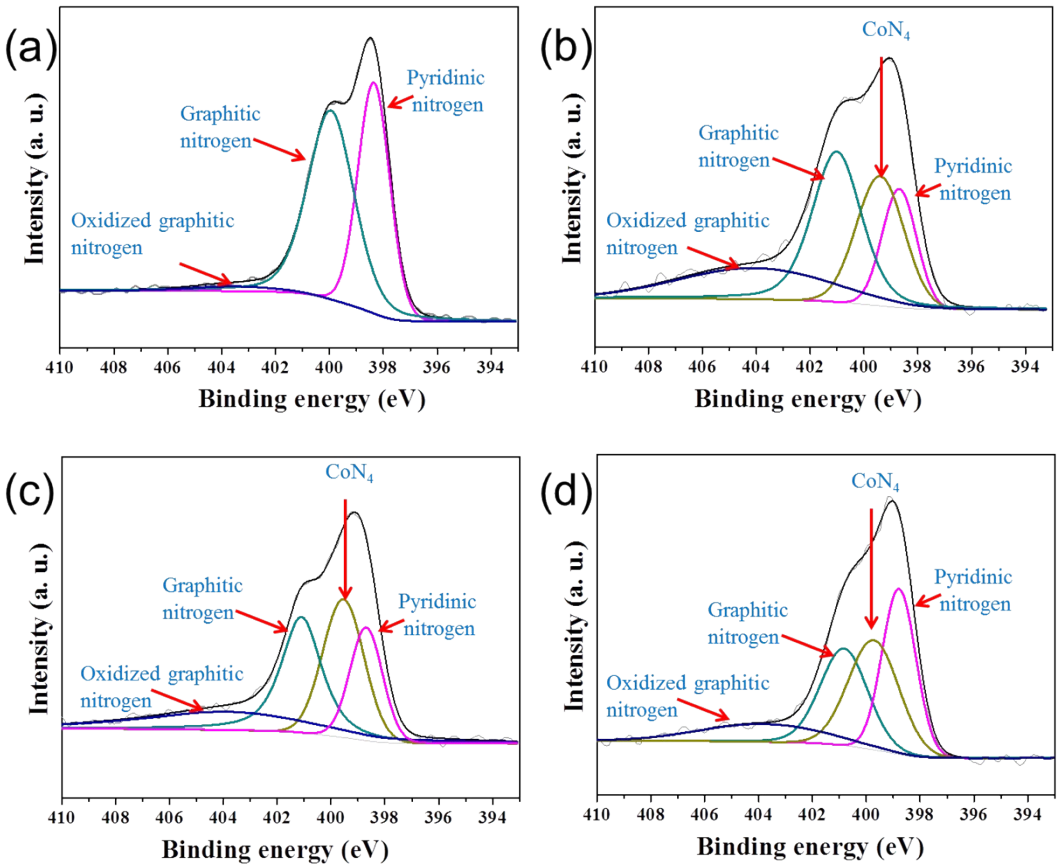

Figure S13. N 1s spectra of Pd@CN(1:0) (a), Pd@CN(1:3) (b), Pd@CN(0:1) (c), Pd@CN(1:3)-650 (d)

There are three types of N in all catalysts: pyridinic N (398.7 eV), graphitic N (401 eV) and oxidized graphitic N (403.9 eV), and the CoN_4 (399.5 eV) only exists in Co-containing catalysts (**Figure** S13).[7] Pd@CN(1:0)-750 contains the highest relative and total contents of graphitic nitrogen and pyridinic nitrogen (**Figure** S14). Pd@CN(1:3)-750 and Pd@CN(0:1)-750 catalysts show no significant difference in the relative percentage of oxidized graphite N. The contents of pyridinic N and CoN_4 of Pd@CN(1:3)-750 are lower than those of Pd@CN(0:1)-750, because the Co NPs in Pd@CN(0:1)-750 are too large to catalyze the formation of graphitic materials (**Figure** S4k).[3, 8] The contents of pyridinic nitrogen and CoN_4 of Pd@CN(1:3)-650 are higher than those of Pd@CN(1:3)-750, because higher temperature is more conducive to increasing the graphitization degree and the volatilization of nitrogen source.[5, 6, 9]

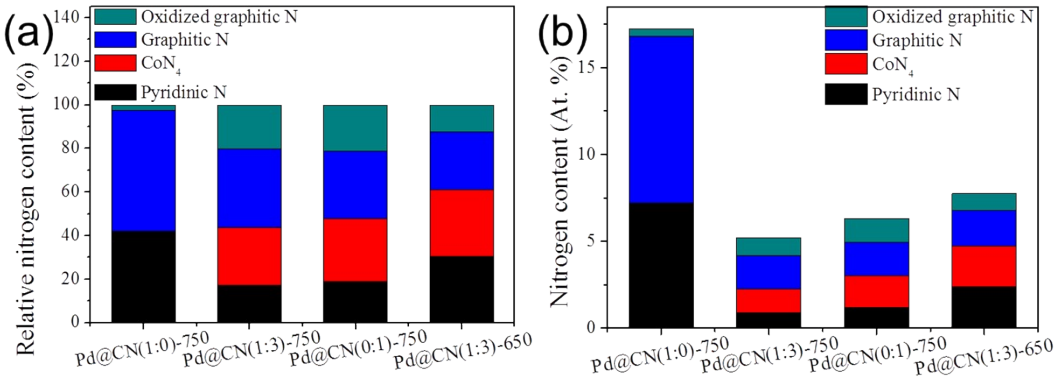

Figure S14. Nitrogen relative content (a) and content of each N-species (b)

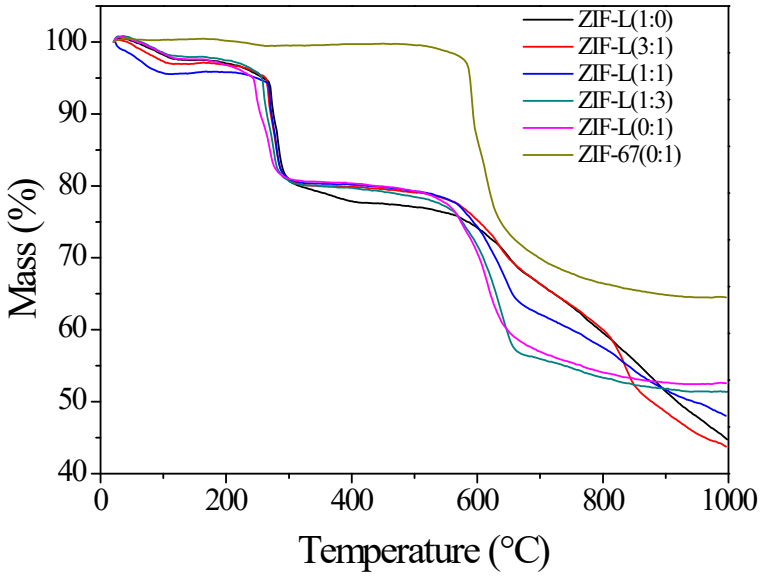

Figure S15. TGA curves of ZIF-L(x:y) and ZIF-67(0:1)

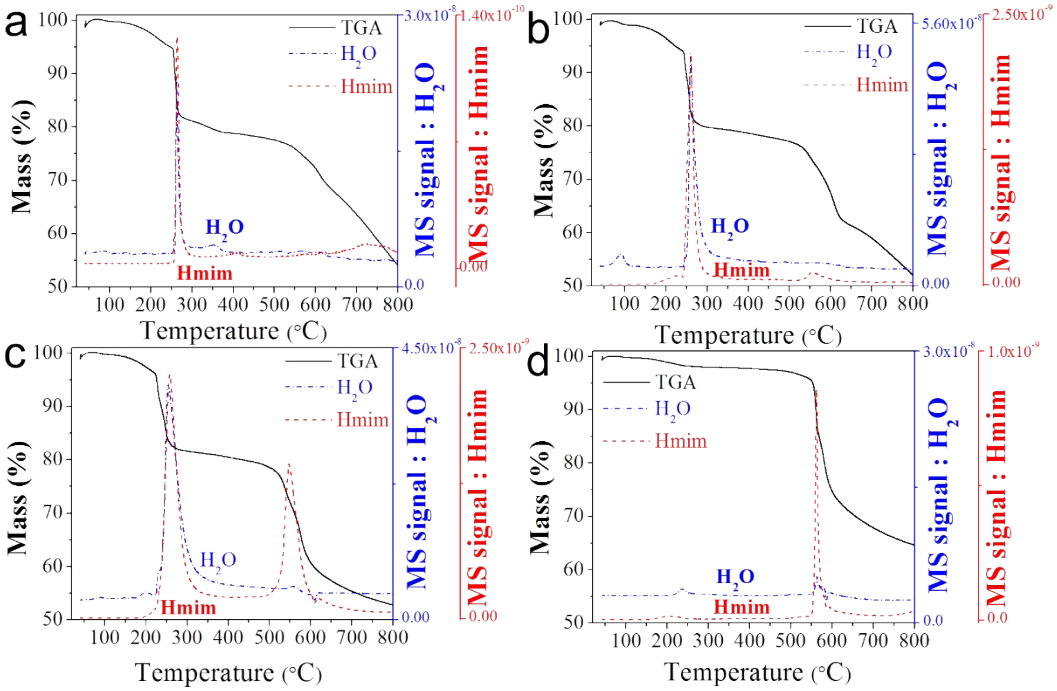

Figure S16. TGA-MS results of ZIF-L(1:0) (a), ZIF-L(1:1) (b), ZIF-L(0:1) (c) and 3D ZIF-67(0:1) (d)

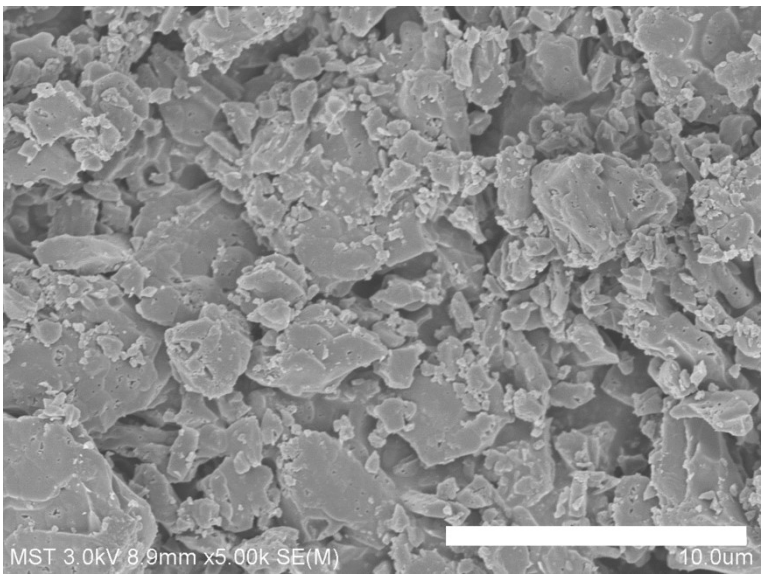

Figure S17. FESEM image of M/CN(1:0)-300

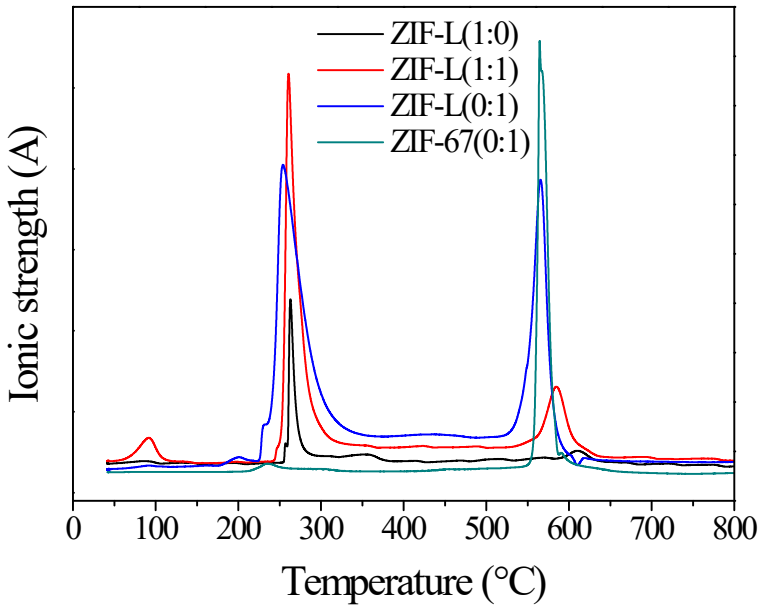

Figure S18. TGA-MS results of ZIF-L(x:y) and ZIF-67(0:1) under thermal treatment (NH_3 signal)

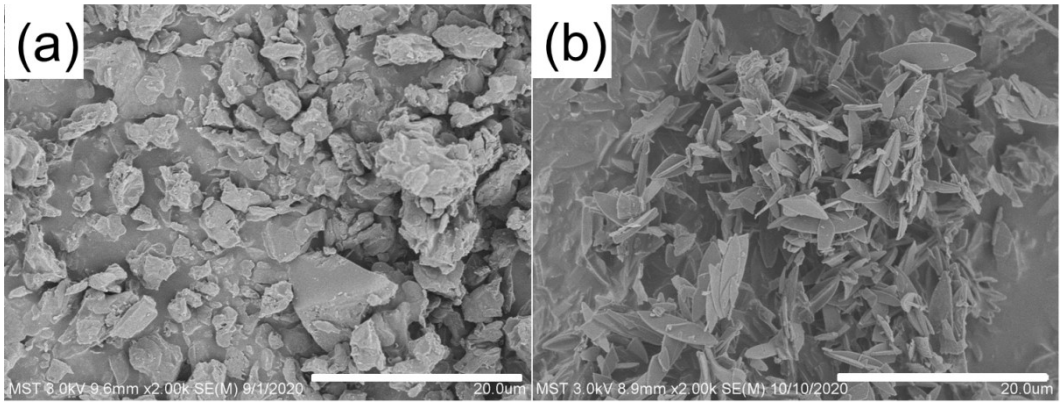

Figure S19. FESEM images of M/CN(0:1)-750. Calcination conditions: 1 g of ZIF-L(0:1) in a porcelain boat (60 mm × 120 mm) at (a) Ar and (b) vacuum (Scale bar = 20 μm)

The mechanism for the morphological transformation of ZIFs during pyrolysis is investigated. All ZIFs (ZIF-L and ZIF-67) show obvious weight loss at around 550 °C, which is caused by the decomposition and transformation of organics (**Figure** S15).[6] The rapid weight loss of ZIFs, which are synthesized with Co source, is due to the decomposition and the direct volatilization of Hmim in the skeleton (**Figure** S16).[6] ZIF-L(1:0) shows little Hmim volatilization in this temperature range, and the weight loss is on account of the transformation of the organic components into CN materials (**Figure** S16a).[6] The morphology of ZIF-L(1:0) is destroyed when calcinated at 300 °C (**Figure** S17), which reveals that the difference in the morphology of the

catalysts occurs at 300 °C or lower temperature.[10] The results in **Figure** S16a-c suggest that the weight loss of ZIF-L at around 250 °C is caused by the volatilization of water and Hmim,[1, 10] which is not detected in the 3D ZIF-67 owing to its higher stability (**Figure** S16d).

Based on the morphological and thermostability studies, for the ZIF-L(x:y) where Zn accounts for more than 50% of the total metal, when the temperature rises to 250 °C, the H_2O, "free" Hmim and Hmim weakly coordinated with Zn are volatilized. Thus, the skeleton of ZIF-L is broken and the morphology is destroyed (**Figures** S4a, b and S16a). On the contrary, when the molar ratio of Zn/Co equals or is lower than 0.5, the Co enhances the interaction between the metal and Hmim. Furthermore, the Co^{2+} in ZIFs is reduced into metal Co, which can catalyze the transformation of Hmim to the more stable carbon materials during the thermal treatment (**Figure** S4c-l).[11, 12] Further heating up to 550 °C leads to the conversion of the Hmim strongly coordinated with Zn into CN. Obvious NH_3 signals are detected at about 550 °C for ZIF(x:y) (y > 0), while no NH_3 is detected at about 550 °C for ZIF-L(1:0) (**Figure** S18). This result reveals that the Hmim strongly coordinated with Zn in ZIF-L(1:0) is less volatile. The retained Hmim is difficult to decompose into NH_3 when the calcination temperature is higher than 550 °C.

The environment for the pyrolysis of ZIF-L(0:1) is critical to the retainment of the 2D nanostructure of M/CN(0:1). The M/CN(0:1), which is prepared by pyrolyzing 1 g of ZIF-L(0:1) in a porcelain boat (60 mm × 120 mm) under Ar atmosphere at 750 °C, bonds together after calcination and the morphology is 3D irregular (**Figure** S19a); on the other hand, when the system is kept in a vacuum state, the resulting product can maintain the 2D morphology (**Figure** S19b). To prevent the "free" Hmim from converting into a "cross-linking agent" that bonds carbon layers together during the calcination, vacuum is important to the volatilization of "free" Hmim. The high mass of precursor in the container shows a negative effect on the volatilization of "free" Hmim, thence carbon layers bond together, and 3D CN materials with irregular morphology are produced.[13-15]

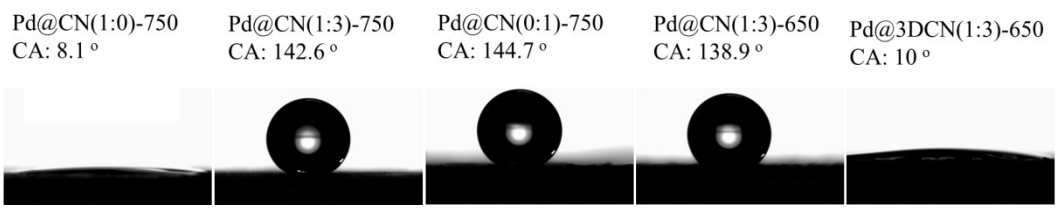

Figure S20. Contact angles of Pd@CN(x:y) and Pd@3DCN(1:3)-650

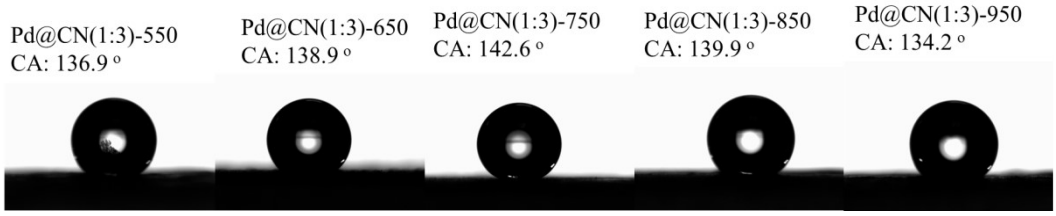

Figure S21. Contact angles of Pd@CN(1:3)-T

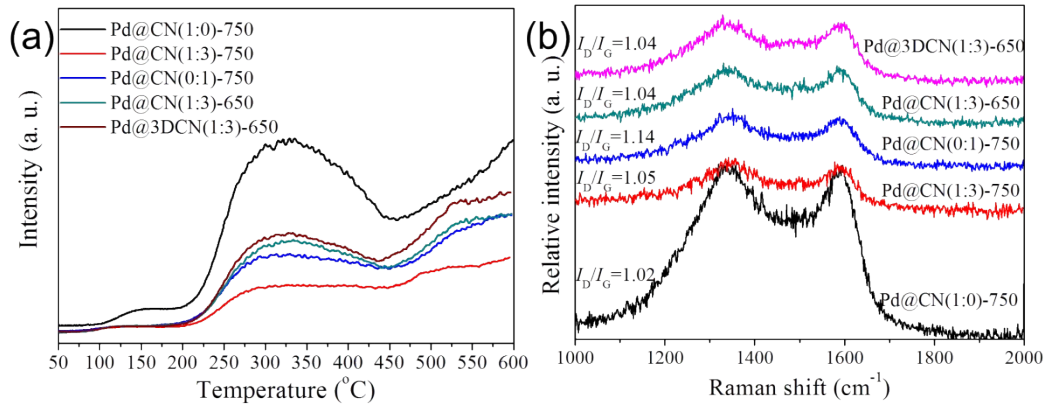

Figure S22. CO_2-TPD patterns (a) and Raman spectra (b) of Pd@CN(x:y) and Pd@3DCN(1:3)-650

All catalysts show an obvious broad peak at around 300 °C (**Figure** S22a), which corresponds to the weak basic sites with a large distribution range.[16] The relative intensity of basic sites shows the following trend: Pd@CN(1:3) < Pd@CN(0:1) < Pd@CN(1:3)-650 < Pd@CN (1:0), which is completely consistent with the trend of N content in the catalysts, suggesting that the N in the catalyst is the important source of its basic sites.[17] The obvious rising peak at temperature higher than 500 °C is caused by the pyrolysis of the catalysts.[17] All catalysts show the D and G bands (**Figure** S22b),[15, 18] and the I_D/I_G values are all higher than 1, suggesting that the Pd@CN catalysts all have abundant defects.[18]

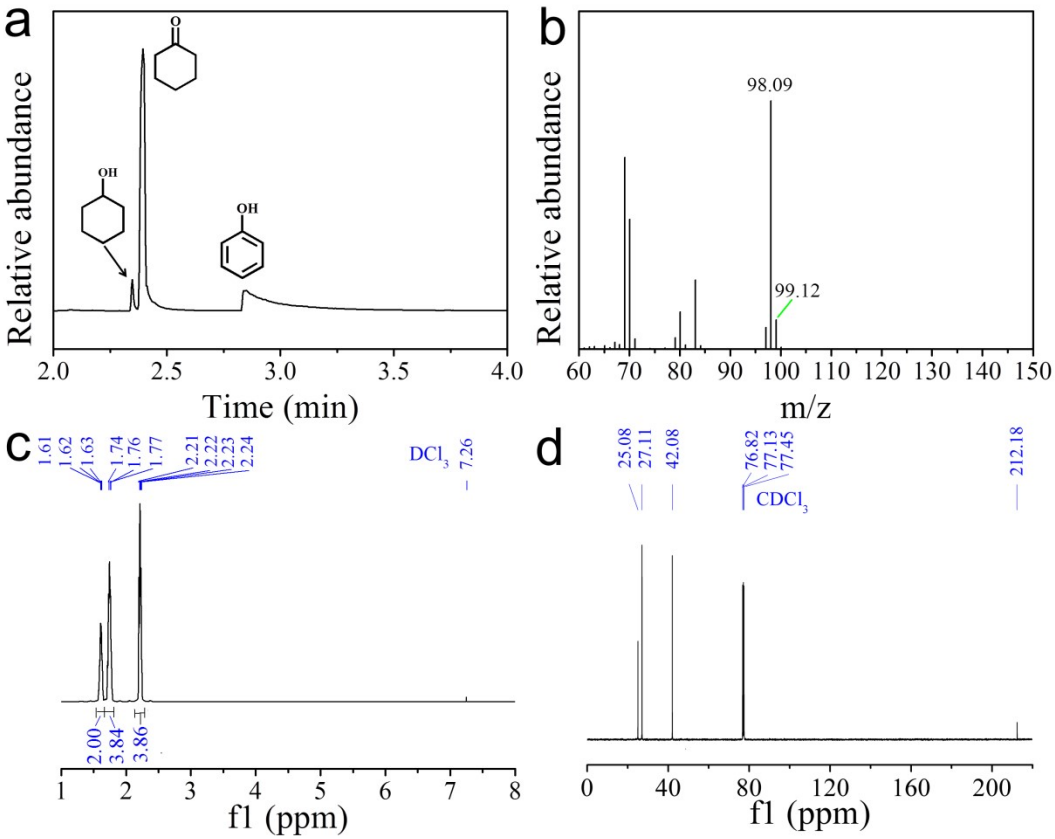

Figure S23. GC-MS result of the reaction liquid (a); mass spectrometry (b), ^{1}H-NMR (c) ^{13}C-NMR (d) of the major product

The MS spectrometry reveals that the composition of the major product is $C_6H_{10}O$; combined with the NMR results, ^{1}H-NMR (400 MHz, $CDCl_3$) δ = 2.33–2.15 (m, 4 H), 1.82–1.71 (m, 4 H), 1.67–1.57 (m, 2 H) and ^{13}C-NMR (400 MHz, $CDCl_3$) δ = 25.08, 27.11 (2C), 42.08 (2C), 212.18, we can confirm that the major product of selective phenol hydrogenation is cyclohexanone.

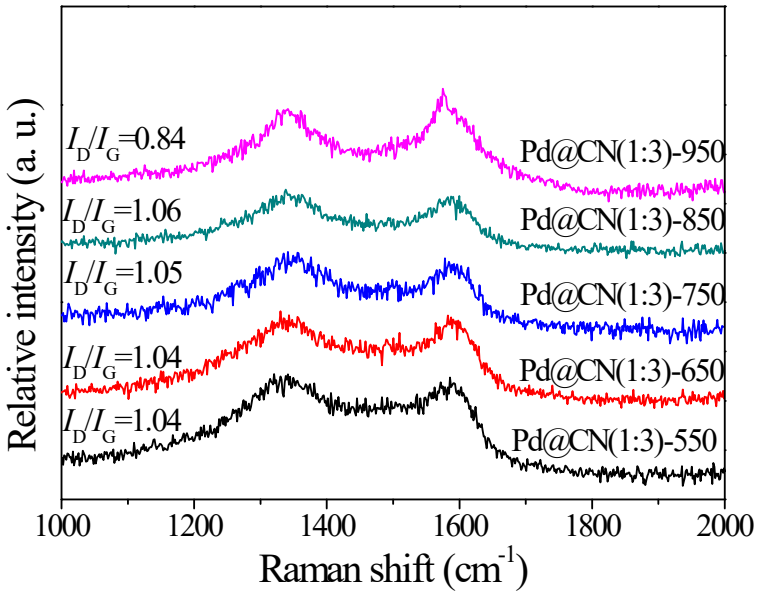

Figure S24. Raman spectra of Pd@CN (1:3)-T

The Pd@CN(1:3)-T catalysts show no significant difference in defects in the calcination temperatures range from 550 to 850 °C (**Figure** S24). The calcination temperature of 950 °C is too high to produce ZIF-derived carbon with rich defects.

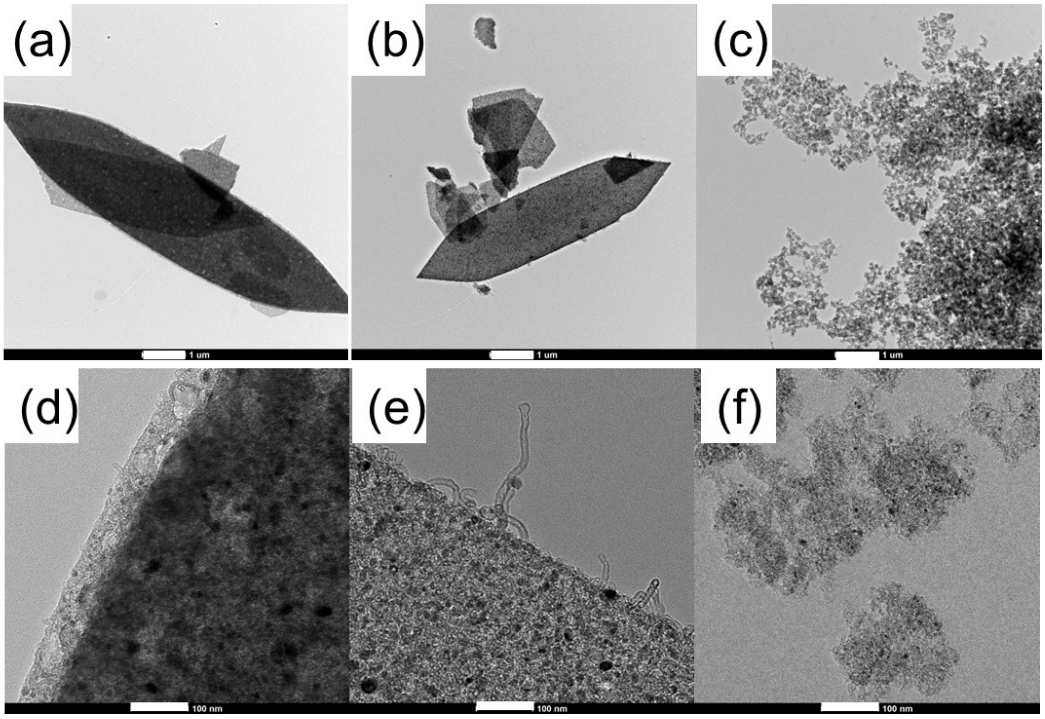

Figure S25. TEM images of (a, d) Pd@CN(0:1)-750, (b, e) Pd@CN(1:3)-650, and (c, f) Pd@3DCN(1:3)-650. (Scale bar in a-c= 1 μm, d-f= 100 nm)

The CNTs on Pd@CN(0:1)-750 are short and few, while the CNTs on Pd@CN(1:3)-650 are more and longer due to the fine size of Co NPs (**Figure** S25). In the transmission state, the 3D ZIF derived Pd@3DCN(1:3)-650 shows the morphology of irregular polyhedron assembled by small nanoparticles.

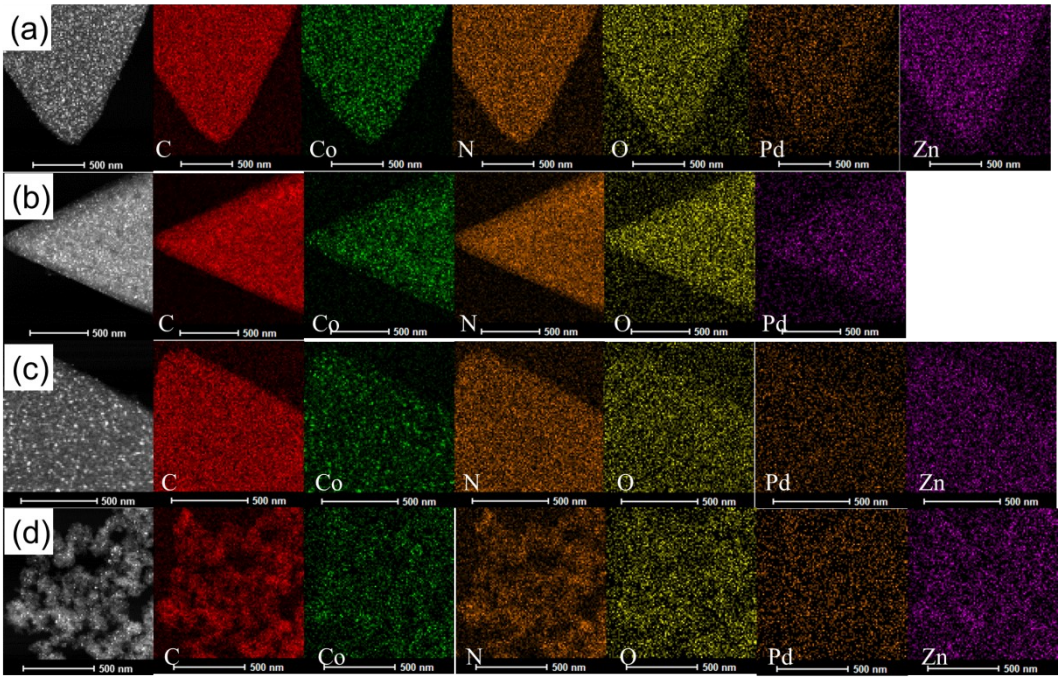

Figure S26. HAADF-STEM images of Pd@CN(1:3)-750 (a), Pd@CN(0:1)-750 (b), Pd@CN(1:3)-650 (c), Pd@3DCN(1:3)-650 (d) and the corresponding mapping images

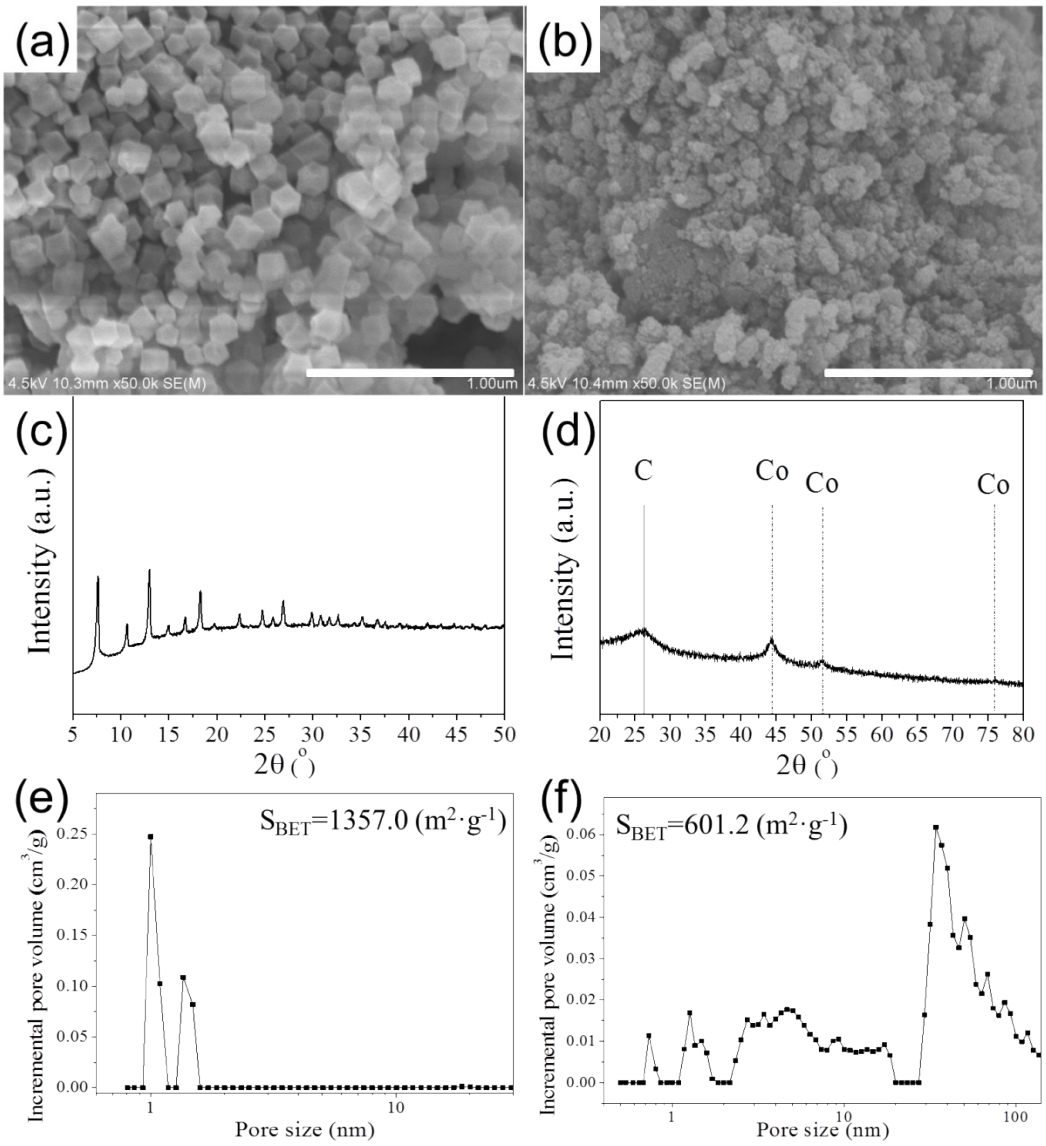

Figure S27. FESEM image (a), XRD pattern (c), and pore size distribution (e) of ZIF-67(1:3); FESEM image (b), XRD pattern (d), and pore size distribution (f) of Pd@3DCN(1:3)-650. (Scale bar in a, b= 1 μm)

ZIF-67(1:3) has a rhombic dodecahedron shape with a particle size of about 100 nm. The polyhedral morphology of ZIF-67(1:3) is destroyed after calcination (**Figures** S25c and S27b), which may be attributed directly to the framework-decoupling-assisted migration of the Zn metal centers into the pore cavities and subsequent ligand decomposition, evolution of N, and evaporation of Zn.[6] There are no CNTs on the surface of the material, possibly because of the embedding of Co NPs in the bulk. The pores larger than 30 nm of Pd@3DCN(1:3)-650 may be formed by the accumulation of small-size CN materials (**Figures** S25f and S27f).

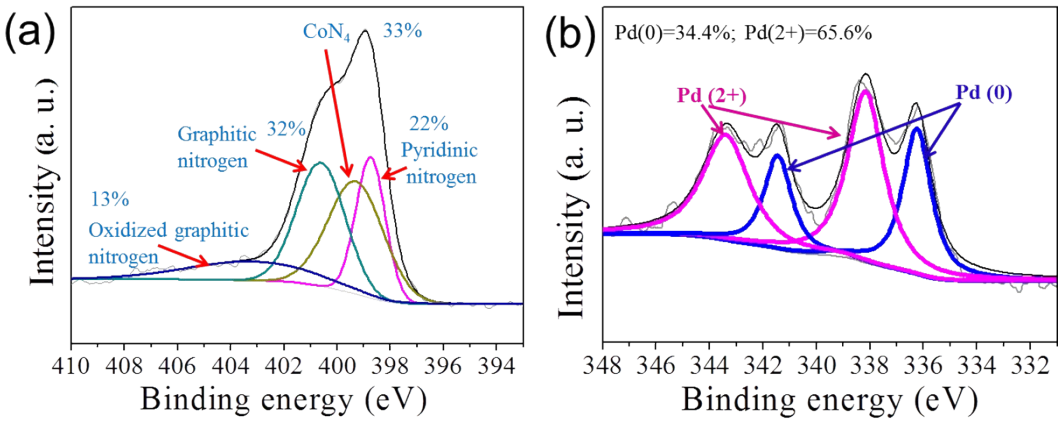

Figure S28. N 1s (a) and Pd 3d (b) spectra of Pd@3DCN(1:3)-650

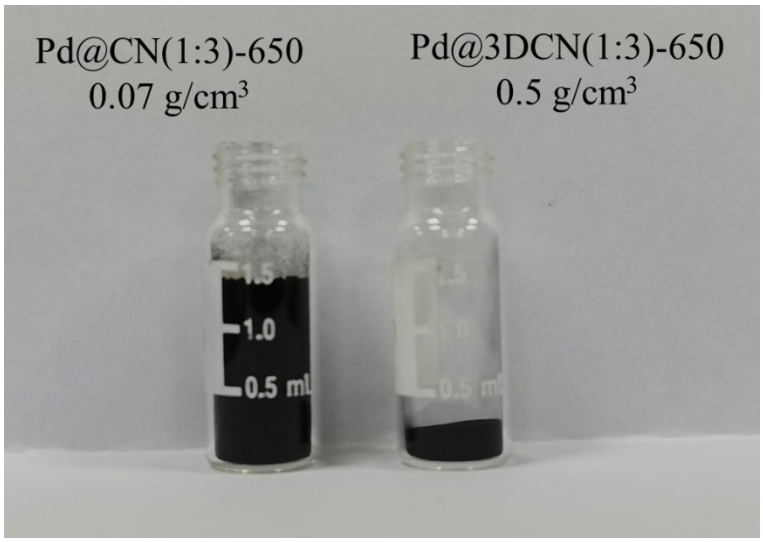

Figure S29. Comparison of the volumes occupied by 0.1 g of Pd@CN(1:3)-650 and 0.1 g of Pd@3DCN(1:3)-650 in powder

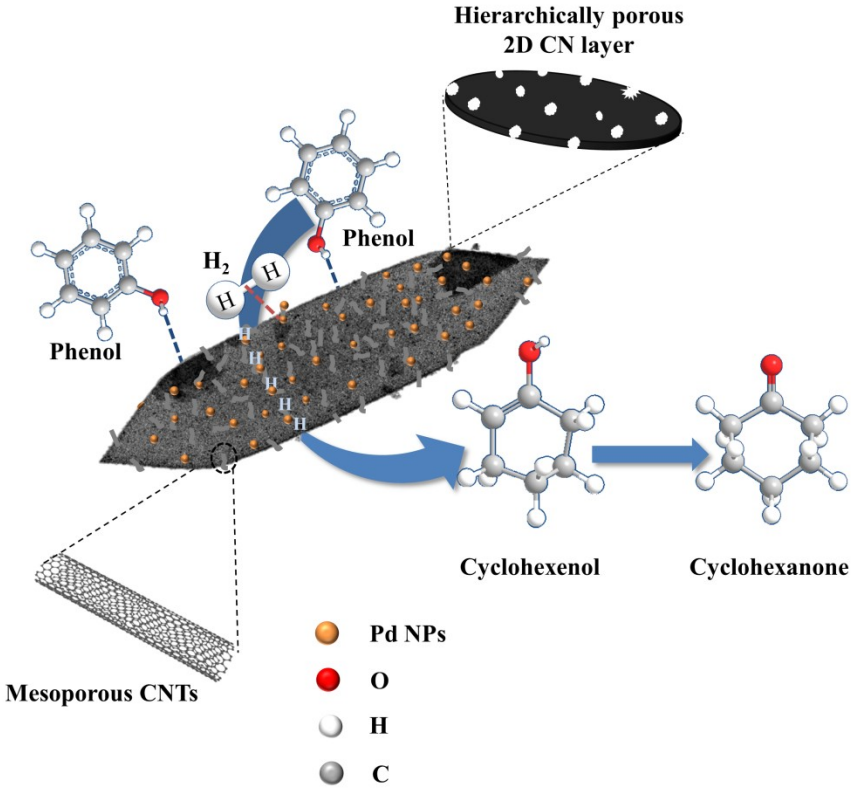

Figure S30. Reaction mechanism of phenol hydrogenation over Pd@CN(1:3)-650

Based on the characterizations results, the possible mechanism of Pd@CN(1:3)-650 with superior catalytic performance for the phenol hydrogenation is suggested. Firstly, the CN(1:3)-650 material with high phenol adsorption capacity (caused by high specific surface area and well-developed hierarchically porous structures) and basic sites (owing to high N content) can gather more phenol on the catalyst surface in the non-planar configuration (**Figures** S11, S22a and Tables S3, S4).[19] It is universally acknowledged that the phenol with two types of adsorption configurations interacts with the support surface: non-planar and co-planar.[20] The co-planar adsorption configuration is in favor of complete hydrogenation to cyclohexanol. In contrast, the non-planar adsorption configuration tends to form partial hydrogenation product cyclohexanone. Secondly, the N in CN(1:3)-650 possesses nucleation sites for loading Pd NPs, thereby higher Pd dispersion. At the same time, the doping N can strengthen the antioxidizability of Pd (**Figures** S12-S14).[5, 17] Pd NPs with good dispersion and high ratio of Pd^0 can accelerate the activation of hydrogen. Thirdly, the well-developed hierarchically porous structures, low dimension and low density of Pd@CN(1:3)-650 make phenol transport faster and active sites more accessible (**Figures** S8, S10). Fourthly, the adsorbed phenol transforms into cyclohexenol (partial

hydrogenation of benzene ring) due to the attack of active hydrogen, then the enol isomerizes quickly to produce cyclohexanone. Lastly, during the phenol hydrogenation, phenol is easily absorbed on the catalyst surface with basic sites, through the hydroxyl group to form strong O-H···N or O-H···π interactions. At the same time, there is only a weaker H-bridge donor between the formed cyclohexanone and the catalyst surface.[20] Therefore, the formed cyclohexanone leaves the catalyst surface rapidly, avoiding further hydrogenation to cyclohexanol and leading to high cyclohexanone selectivity.

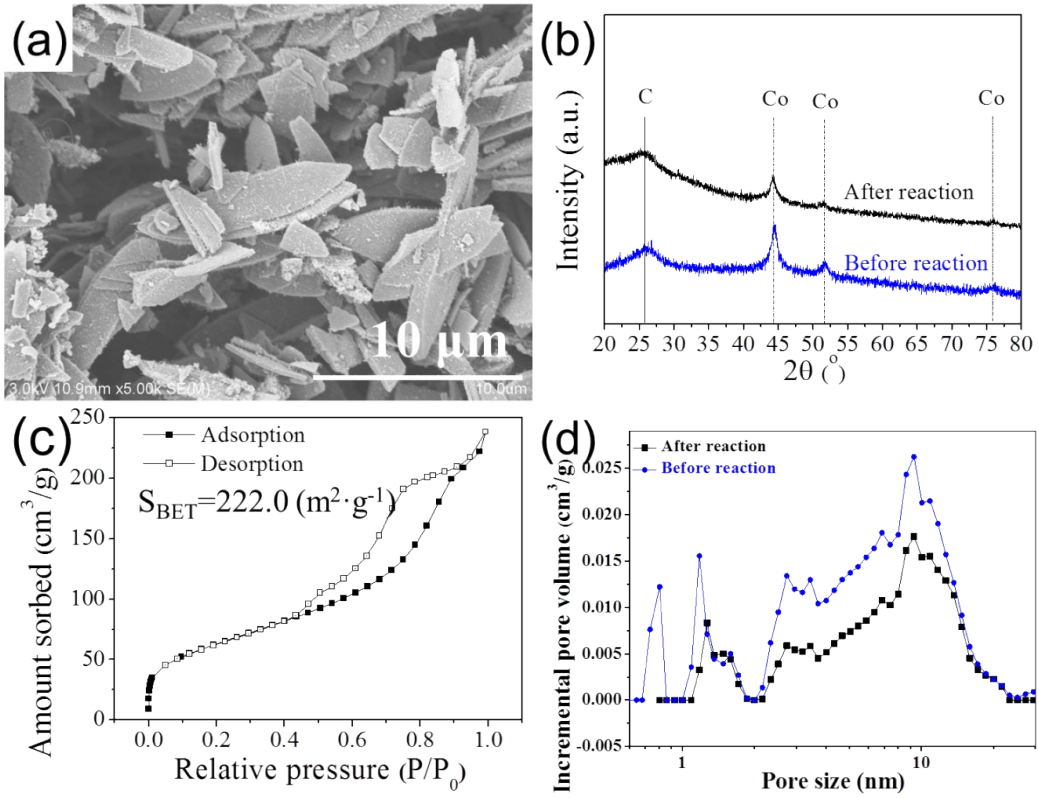

Figure S31. FESEM image (a), XRD pattern (b), N_2 sorption isotherms (c) and pore size distribution (d) of the Pd@CN(1:3)-650 catalyst after four reaction cycles

Table S1. Textural properties of M/CN(x:y)

Samples	S_{BET} (m^2 g^{-1})	S_{mic} (m^2 g^{-1})	S_{extra}/S_{BET}	V_{total} (cm^3 g^{-1})	V_{mic} (cm^3 g^{-1})	V_{extra}/V_{total}
M/CN(1:0)-750	595.8	570.2	0.04	0.26	0.22	0.15
M/CN(3:1)-750	504.7	486.8	0.04	0.25	0.2	0.20
M/CN(1:1)-750	217.9	214.6	0.02	0.11	0.09	0.18
M/CN(1:3)-750	300.8	216.1	0.28	0.39	0.06	0.85
M/CN(0:1)-750	222.4	207.4	0.07	0.13	0.09	0.31

$S_{extra}= S_{BET}- S_{mic}$; $V_{extra}= V_{total}- V_{mic}$

Table S2. Textural properties and Pd loading of Pd@CN(x:y)

Catalysts	S_{BET} (m^2 g^{-1})	S_{mic} (m^2 g^{-1})	S_{extra}/S_{BET}	V_{total} (cm^3 g^{-1})	V_{mic} (cm^3 g^{-1})	V_{extra}/V_{total}	Pd loading (wt %)
Pd@CN(1:0)	790.0	725.8	0.08	0.38	0.30	0.21	1.2
Pd@CN(3:1)	422.8	370.7	0.12	0.27	0.16	0.41	0.8
Pd@CN(1:1)	452.1	274.0	0.39	0.35	0.14	0.6	1.1
Pd@CN(1:3)	464.2	122.9	0.74	0.56	0.06	0.89	1.4
Pd@CN(0:1)	359.5	274.0	0.24	0.3	0.14	0.53	1.4

$S_{extra}= S_{BET}- S_{mic}$; $V_{extra}= V_{total}- V_{mic}$

Table S3. Textural properties and Pd loading of Pd@CN(1:3)-T

Calcination temperature (°C)	S_{BET} (m^2 g^{-1})	S_{mic} (m^2 g^{-1})	S_{extra}/ S_{BET}	V_{total} (cm^3 g^{-1})	V_{mic} (cm^3 g^{-1})	V_{extra}/ V_{total}	Pd loading (wt. %)
550	241.9	23	0.90	0.35	0.01	0.97	0.3
650	440.7	175.9	0.60	0.55	0.08	0.85	0.9
750	464.2	122.9	0.74	0.56	0.06	0.89	1.4
850	556.5	145.5	0.74	0.72	0.08	0.89	1.5
950	407.0	85.2	0.79	0.57	0.07	0.88	1.7

$S_{extra}= S_{BET}- S_{mic}$; $V_{extra}= V_{total}- V_{mic}$

Table S4. Phenol adsorption capacities of different catalysts

Catalysts	Phenol adsorption capacities（g g^{-1}）
Pd@CN(1:3)-550	0.39
Pd@CN(1:3)-650	0.3
Pd@CN(1:3)-750	0.19
Pd@CN(1:3)-850	0.05
Pd@CN(1:3)-950	0.2

Table S5. Elements content of Pd@3DCN(1:3)-650

Measurements	C 1s	N 1s	O 1s	Co 2p	Zn 2p	Pd 3d
XPS (At. %)	83.87	9.82	4.78	0.97	0.23	0.33
ICP (wt. %)						0.99

Table S6. Catalytic performance of various Pd-based catalysts applied to the phenol hydrogenation[A]

Catalysts	n_{Pd}:n_{phenol} (%)	Reaction conditions				Conversion (%)	Selectivity (%)	TOFs (h^{-1})[D]	References
		Phenol addition (mmol)	Volume (mL)	Temperature (°C)	Time (min)				
Pd1.2@CN-rGO-15[B]	2.1	0.53	5	80	80	97.2	96.7	33.7	[15]
Pd@mpg-C_3N_4[B]	5	0.5	2	65	120	>99.9	>99.9	9.9	[20]
Pd@mpg-C_3N_4[B]	4	0.59	2	65	360	100	100	4.17	[21]
Na-Pd/TiO_2[B]	0.44	5.32	20	80	360	>99	>99	37.13	[22]
0.07-Pd/PNCM-800[B]	10	0.25	3	80	180	99	99	3.27	[23]
Pd-PANI/CNT[B]	5	0.43	3	80	480	86	99	2.13	[24]
Pd/$N_{4.8}$-meso-CNRs[B]	3	0.5	2	40	180	93.2	97.3	10.1	[25]
[a]1Pd/HAP-SSD[B]	5	0.05	2	85	300	97.9	96.5	3.8	[26]
Pd−chitin-150[B]	5	0.5	3	90	120	100	100	0.1	[27]
Pd@HMSNs[B]	3	0.1	4	55	240	99.0	98.3	7.6	[28]
Pd/MIL-101[B]	5	1	4	30	600	>99.9	>99.9	1.99	[29]
Pd@sMMT-1[B]	1.5	0.5	2	25	900	99	98	4.31	[30]
Pd^5@FDU^3–N^H [B]	5	0.5	2	100	60	80	>99	15.84	[31]

Catalysts	$n_{Pd}:n_{phenol}$ (%)	Reaction conditions				Conversion (%)	Selectivity (%)	TOFs (h^{-1})[D]	References
		Phenol addition (mmol)	Volume (mL)	Temperature (°C)	Time (min)				
Pd/NH_2-SBA-15[B]	2	0.5	10	80	120	98.0	99.6	24.4	[32]
Pd@CN-TiO_2-25[B]	6.1	0.53	5	80	70	98.0	98.0	13.49	[33]
Pd@CN@TiO_2-8-450[B]	3.2	0.54	5	80	60	98	98.3	30.1	[34]
Pd@CN(1:3)-550[B]	0.05	1.66	20	80	120	0.57	100	5.7	This work
Pd@3DCN(1:3)-650[B]	0.17	1.66	20	80	120	16.4	94.3	45.5	This work
Pd@CN(1:3)-650[B]	0.16	1.66	20	80	120	25.4	92.7	73.6	This work
Pd@CN(1:3)-750[B]	0.24	1.66	20	80	120	68.6	85.6	122.3	This work
Pd@CN(1:3)-550[C]	0.05	1.66	20	80	120	2.33	100	25.2	This work
Pd@3DCN(1:3)-650[C]	0.17	1.66	20	80	120	72.5	97.5	210.6	This work
Pd@CN(1:3)-650[C]	0.16	1.66	20	80	120	94.0	94.7	276.5	This work
Pd@CN(1:3)-750[C]	0.24	1.66	20	80	120	88.1	94.1	172.1	This work

[A]Pressure of H_2 is 1 bar; [B]Water as the solvent; [C]Cyclohexane as the solvent; [D] TOFs are calculated by moles of cyclohexanone/(moles of Pd* reaction time).

Table S7. Catalytic performance of different catalysts for the reduction of nitroarenes and phenol derivatives

Entry	Substrates	Catalysts	Time (min)	Conversion (%)	Major products	Selectivity (%)
1 [a]	*o*-benzenediol	Pd@CN(1:3)-650	120	6.07	2-Hydroxycyclohexanone	94.95
		Pd@3DCN(1:3)-650	120	2.34		100
2 [a]	*m*-benzenediol	Pd@CN(1:3)-650	120	20.85	1, 3-Cyclohexanedione	64.86
		Pd@3DCN(1:3)-650	120	16.02		56.17
3 [a]	*p*-benzenediol	Pd@CN(1:3)-650	120	46.87	4-Hydroxycyclohexanone	96.48
		Pd@3DCN(1:3)-650	120	6.76	1, 4-Cyclohexanediol	98.55
7 [b]	*p*-Nitrophenol	Pd@CN(1:3)-650	4	86.6	*p*-Aminophenol	100
		Pd@3DCN(1:3)-650	4	83.3		100
8 [b]	*o*-Nitrophenol	Pd@CN(1:3)-650	0.5	100	*o*-Aminophenol	100
		Pd@3DCN(1:3)-650	2.5	100		100
9 [c]	*p*-Nitrotoluene	Pd@CN(1:3)-650	1	76.6	*p*-Aminotoluene	100
		Pd@3DCN(1:3)-650	1	33.9		100
10 [c]	*p*-Nitrobenzoic acid	Pd@CN(1:3)-650	1	76.7	*p*-Aminobenzoic acid	100
		Pd@3DCN(1:3)-650	1	24.5		100

[a] Reaction conditions: substrates (0.2 g), H_2 (0.1 MPa), water (20 mL), catalyst (0.03 g), reaction temperature (80 °C).

[b] Reaction conditions: substrates (0.2 g), $NaBH_4$ (0.5 g), ethanol (50 mL), catalyst (0.03 g), reaction temperature (30 °C).

[c] Reaction conditions: substrates (0.4 g), $NaBH_4$ (0.5 g), ethanol (90 mL), catalyst (0.03 g), reaction temperature (30 °C).

Table S8. Elements content of reaction liquid after filtration

Measurement	Co	Zn	Pd
ICP (mg L^{-1})	0.020	0.003	0.014

Supplementary references

1 R. Z. Chen, J. F. Yao, Q. F. Gu, S. Smeets, C. Baerlocher, H. X. Gu, D. R. Zhu, W. Morris, O. M. Yaghi and H. T. Wang, *Chem. Commun.,* 2013, **49**, 9500-9502.

2 X. J. Wang, J. W. Zhou, H. Fu, W. Li, X. X. Fan, G. B. Xin, J. Zheng and X. G. Li, *J. Mater. Chem. A,* 2014, **2**, 14064-14070.

3 B. You, N. Jiang, M. Sheng, W. S. Drisdell, J. Yano and Y. J. Sun, *ACS Catal.,* 2015, **5**, 7068-7076.

4 G. F. Hu, L. Shang, T. Sheng, Y. G. Chen and L. Y. Wang, *Adv. Funct. Mater.,* 2020, **30**, 2002281.

5 S. S. Ding, C. H. Zhang, Y. F. Liu, H. Jiang, W. H. Xing and R. Z. Chen, *J. Ind. Eng. Chem.,* 2017, **46**, 258-265.

6 J. Cheng, N. Liu, Y. L. Wang, X. X. Xuan, X. Yang and J. H. Zhou, *Fuel,* 2020, **265,** 116972.

7 Y. H. He, S. Y. Hwang, D. A. Cullen, M. A. Uddin, L. Langhorst, B. Y. Li, S. Karakalos, A. J. Kropf, E. C. Wegener, J. Sokolowski, M. J. Chen, D. Myers, D. Su, K. L. More, G. F. Wang, S. Litster and G. Wu, *Energ. Environ. Sci.,* 2019, **12**, 250-260.

8 A. Gohier, C. P. Ewels, T. M. Minea and M. A. Djouadi, *Carbon,* 2008, **46**, 1331-1338.

9 Y. Q. Wu, X. C. Qiu, F. Liang, Q. K. Zhang, A. Koo, Y. N. Dai, Y. Lei and X. L. Sun, *Appl. Catal. B: Environ.,* 2019, **241**, 407-414.

10 Z. X. Zhong, J. F. Yao, Z. X. Low, R. Z. Chen, M. He and H. T. Wang, *Carbon,* 2014, **72**, 242-249.

11 R. M. Zhu, J. W. Ding, J. P. Yang, H. Pang, Q. Xu, D. L. Zhang and P. Braunstein, *ACS Appl. Mater. Inter.*, 2020, **12**, 25037-25041.

12 Z. Yu, Y. Bai, S. M. Zhang, Y. X. Liu, N. Q. Zhang, G. H. Wang, J. H. Wei, Q. B. Wu and K. N. Sun, *ACS Appl. Mater. Inter.,* 2018, **10**, 6245-6252.

13 M. Ciprian, K. H. Ruiz, M. Kassymova, T. T. Wang, S. Zhuiykov, S. Chaemchuen, R. Tu and F. Verpoort, *Micropor. Mesopor. Mat.,* 2019, **285**, 80-88.

14 X. Q. Xu, F. T. Ran, Z. M. Fan, H. Lai, Z. J. Cheng, T. Lv, L. Shao and Y. Y. Liu, *ACS Appl. Mater. Inter.,* 2019, **11**, 13564-13573.

15 J. X. Zhang, C. H. Zhang, H. Jiang, Y. F. Liu and R. Z. Chen, *Ind. Eng. Chem. Res.,* 2020, **59**, 10768-10777.

16 H. Jiang, Z. Y. Qu, Y. Li, J. Huang, R. Z. Chen and W. H. Xing, *Chem. Eng. J.,* 2016, **284**, 724-732.

17 Y. L. Cao, S. J. Mao, M. M. Li, Y. Q. Chen and Y. Wang, *ACS Catal.,* 2017, **7**, 8090-8112.

18 T. T. Sun, Y. L. Li, T. T. Cui, L. B. Xu, Y. G. Wang, W. X. Chen, P. P. Zhang, T. Y. Zheng, X. Z. Fu, S. L. Zhang, Z. D. Zhang, D. S. Wang and Y. D. Li, *Nano Lett.,* 2020, **20**, 6206-6214.

19 X. Q. Kong, Y. T. Gong, S. J. Mao and Y. Wang, *ChemNanoMat,* 2018, **4**, 432-450.

20 Y. Wang, J. Yao, H. R. Li, D. S. Su and M. Antonietti, *J. Am. Chem. Soc.,* 2011, **133**, 2362-

2365.

21 Y. Li, X. Xu, P. F. Zhang, Y. T. Gong, H. R. Li and Y. Wang, *RSC Adv.,* 2013, **3**, 10973-10982.

22 H. Zhou, B. B. Han, T. Z. Liu, X. Zhong, G. L. Zhuang and J. G. Wang, *Green Chem.,* 2017, **19**, 3585-3594.

23 Y. A. Zhu, G. Q. Yu, J. Yang, M. Yuan, D. Xu and Z. P. Dong, *J. Colloid Interf. Sci.,* 2019, **533**, 259-267.

24 J. Z. Chen, W. Zhang, L. M. Chen, L. L. Ma, H. Gao and T. J. Wang, *ChemPlusChem,* 2013, **78**, 142-148.

25 X. T. Liu, F. Pang and J. P. Ge, *Chem. Asian J.,* 2018, **13**, 822-829.

26 Y. Shen, X. K. Bo, Z. F. Tian, Y. Z. Wang, X. K. Guo, M. J. Xie, F. Gao, M. Lin, X. F. Guo and W. P. Ding, *Green Chem.,* 2017, **19**, 2646-2652.

27 C. C. Zhao, Z. Y. Zhang, Y. R. Liu, N. Z. Shang, H. J. Wang, C. Wang and Y. J. Gao, *ACS Sustain. Chem. Eng.,* 2020, **8**, 12304-12312.

28 C. P. Yang, K. J. Li, J. Y. Wang and S. H. Zhou, *Appl. Catal. A: Gen.,* 2021, **610**, 117961.

29 H. L. Liu, Y. W. Li, R. Luque and H. F. Jiang, *Adv. Synth. Catal.,* 2011, **353**, 3107-3113.

30 C. J. Lin, S. H. Huang, N. C. Lai and C. M. Yang, *ACS Catal.,* 2015, **5**, 4121-4129.

31 Z. L. Li, J. H. Liu, C. G. Xia and F. W. Li, *ACS Catal.,* 2013, **3**, 2440-2448.

32 H. F. Li, T. T. She, G. F. Chen, M. H. Sun, L. B. Niu and G. Y. Bai, *Mol. Catal.,* 2021, **504**, 111493.

33 J. X. Zhang, Y. F. Liu, H. Jiang and R. Z. Chen, *React. Kinet. Mech. Cat.,* 2019, **126**, 463-7.

34 J. X. Zhang, H. Jiang, Y. F. Liu and R. Z. Chen, *Appl. Surf. Sci.,* 2019, **488**, 555-564.